Predicting impact damage, residual strength and crashworthiness of composite structures

2016-01-0497
Published 04/05/2016

doi:10.4271/2016-01-0497
saematman.saejournals.org

Predicting Impact Damage, Residual Strength and Crashworthiness of Composite Structures

Brian Falzon and Wei Tan
Queen's University Belfast

ABSTRACT

The development of the latest generation of wide-body carbon-fibre composite passenger aircraft has heralded a new era in the utilisation of these materials. The premise of superior specific strength and stiffness, corrosion and fatigue resistance, is tempered by high development costs, slow production rates and lengthy and expensive certification programmes. Substantial effort is currently being directed towards the development of new modelling and simulation tools, at all levels of the development cycle, to mitigate these shortcomings. One of the primary challenges is to reduce the extent of physical testing, in the certification process, by adopting a 'certification by simulation' approach. In essence, this aspirational objective requires the ability to reliably predict the evolution and progression of damage in composites. The aerospace industry has been at the forefront of developing advanced composites modelling tools. As the automotive industry transitions towards the increased use of composites in mass-produced vehicles, similar challenges in the modelling of composites will need to be addressed, particularly in the reliable prediction of crashworthiness. While thermoset composites have dominated the aerospace industry, thermoplastics composites are likely to emerge as the preferred solution for meeting the high-volume production demands of passenger road vehicles. This keynote paper outlines recent progress and current challenges in the development of finite-element-based predictive modelling tools for capturing impact damage, residual strength and energy absorption capacity of thermoset and thermoplastic composites for crashworthiness assessments.

CITATION: Falzon, B. and Tan, W., "Predicting Impact Damage, Residual Strength and Crashworthiness of Composite Structures," *SAE Int. J. Mater. Manf.* 9(3):2016, doi:10.4271/2016-01-0497.

INTRODUCTION

Composite materials are finding increasing utilisation in a number of transportation industries concerned with making structures lighter to reduce environmental impact and improve efficiency. Nevertheless, composite structures are susceptible to damage from low-velocity impact events (e.g. accidental damage incurred in service or during routine maintenance). Even with barely visible impact damage, CAI residual strength can be significantly reduced. Another major challenge in the development of land-based mass-transportation fibre-reinforced polymer composite vehicles is ensuring a prescribed level of crashworthiness [1]. While the potential superior energy absorbing capacity of carbon-fibre composite structures is repeatedly demonstrated in Formula One racing [2], the design of a cost-effective crashworthy carbon-fibre reinforced polymer automotive passenger cabin has yet to be realised.

One approach for reducing development time and cost of composite structures is to increase the use of modelling and simulation at all levels of the product development cycle. The aerospace and automotive industries have been at the forefront of integrating modelling and simulation tools into their product development [3], but the shift towards the increased use of composite materials has highlighted the inadequacy of existing simulation tools to reliably predict the structural response of composites under damage-inducing loads. The exhaustive experimental programme, currently required as part of the development and certification of a new composite airframe is testament to this lack of capability. Current practice follows a building block approach which was first represented by Rouchon [4] as a test pyramid. The purpose of adopting this approach is to mitigate risk by progressing through a sequence of testing; starting from simple (generic) coupons, for basic material characterisation, and moving to more complex (non-generic) structural details as shown in Figure 1. This is costly and highly inefficient. The need for replacing some of this physical testing by simulation, as suggested in Figure 1, is equally applicable to the development of automotive composite structures where crashworthiness assessments are critical, placing additional demands on computational requirements.

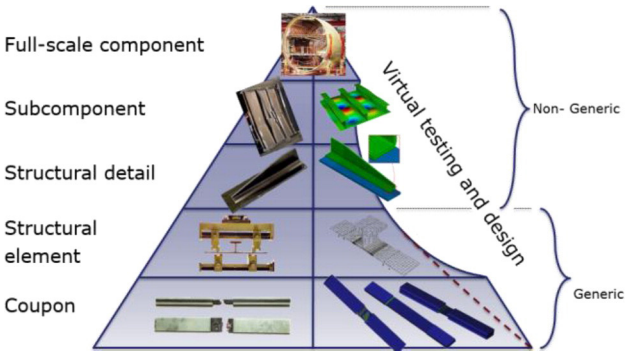

Figure 1. Rouchon pyramid for certification of composite aerostructures.

This paper will focus on recent developments in addressing the challenge of developing a mesoscale finite element based damage model, which builds on the work of Falzon's research group [5,6,7,8,9], for predicting impact damage, residual strength and energy absorption capacity of carbon fibre composites structures.

1. MESOSCALE DAMAGE MODEL

The failure modes exhibited by laminated composites may be classified as intralaminar (matrix cracks and fibre pullout/breakage) and interlaminar (delamination) damage as shown in Figure 2.

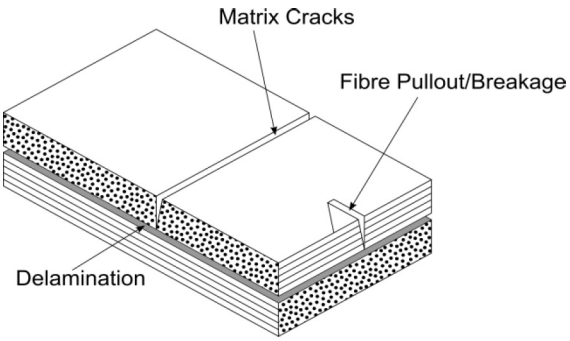

Figure 2. Damage modes in laminated composites.

1.1. Interlaminar Damage Model

The surface-based cohesive behaviour in ABAQUS/Explicit [10] was used to capture delamination using a bilinear traction-separation relationship. This approach is a convenient means to model the cohesive connections without the need to define cohesive elements and tie constraints. Failure initiation was governed by a quadratic stress criterion,

$$\left(\frac{\tau_1}{\tau_1^0}\right)^2 + \left(\frac{\tau_2}{\tau_2^0}\right)^2 + \left(\frac{\langle\tau_3\rangle}{\tau_3^0}\right)^2 \leq 1, \tag{1}$$

where τ_i (i = 1,2,3) are the stresses in the in-plane directions (1,2) and normal direction (3) respectively, and τ_i^0 are the corresponding maximum stresses associated with each direction, $\tau_{sh}^0 = \sqrt{(\tau_1^0)^2 + (\tau_2^0)^2}$. Delamination was propagated using a mixed-mode relationship proposed by Benzeggagh and Kenane (B-K propagation criterion) [11],

$$G_c = G_{Ic} + (G_{IIc} - G_{Ic})\mathrm{B}^{\eta}, \tag{2}$$

where G_c is the mixed-mode fracture toughness, B is the local mixed-mode ratio defined as $B = G_{shear}/(G_I + G_{shear})$. As mode III is not considered, $G_{shear} = G_{II}$. η is the mixed-mode interaction determined from experimental measurements. The mixed-mode softening law is shown in Figure 3.

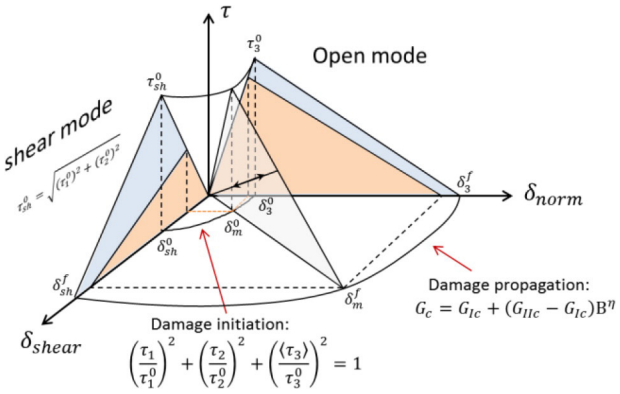

Figure 3. Mixed-mode softening law [12].

1.2. Intralaminar Damage Model

The developed intralaminar damage model is based on a continuum damage mechanics approach proposed by Lemaitre and Chaboche [13], as a method to determine the behaviour of a material under damage-inducing loads. The effective stresses are defined as stresses transmitted across the intact part of the cross-section in a Representative Volume Element (RVE). The damage tensor is a function of three monotonically increasing damage variables, bound by 0 (no damage) and 1 (complete failure), each relating to a form of damage mode under a different loading state; (i) d_{11}^T refers to tensile damage in the fibre direction, (ii) d_{11}^C refers to compressive damage in the fibre direction and (iii) d_{mat} refers to matrix cracking due to a combination of transverse tension/compression and shear loading, which is a unified matrix damage mechanism. The components of the effective stress tensor, $\tilde{\sigma}$, and true stress tensor, σ, can be linked by the damage tensor, $\boldsymbol{D}$, undamaged material elasticity tensor, $\boldsymbol{C}$, and the strain tensor ε,

$$\sigma = \boldsymbol{D}\tilde{\sigma} = \boldsymbol{D}\boldsymbol{C}\varepsilon\,, \tag{3}$$

1.2.1. Non-Linear Shear Damage Model

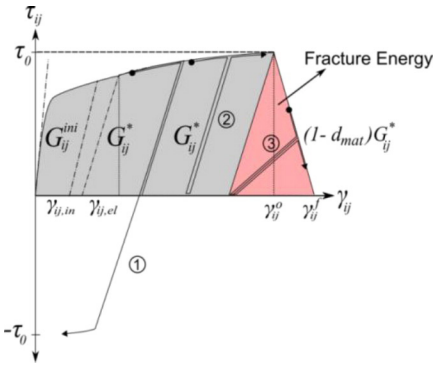

Figure 4. Non-linear shear model.

Considerable plastic shear strain and modulus degradation was observed with several consecutive loading-unloading cycles applied to test specimens. Prior to damage initiation, shear loading and unloading occurs along gradients defined by the initial shear modulus G_{ij}^{ini} and degraded shear modulus G_{ij}^*, shown in Figure 4, respectively. According to plastic-damage theories, the plastic strain

represents all irreversible deformations including those caused by matrix microcracks. The shear strain γ_{ij} was decomposed into the elastic part $\gamma_{ij,el}$ and the inelastic/plastic part $\gamma_{ij,in}$,

$$\gamma_{ij} = \gamma_{ij,el} + \gamma_{ij,in}. \quad i \neq j = 1,2,3 \tag{4}$$

The elastic strain is given by,

$$\gamma_{ij,el} = \tau_{ij}/G^*_{ij}. \tag{5}$$

The stress-strain constitutive laws are represented by an exponential function,

$$\tau_{ij}(\gamma_{ij}) = \begin{cases} \tau^Y_{ij} * \left[exp(\alpha * \gamma_{ij}) - exp(\beta * \gamma_{ij})\right], & \gamma_{ij} \geq 0 \\ \tau^Y_{ij} * \left[-exp(-\alpha * \gamma_{ij}) + exp(-\beta * \gamma_{ij})\right], & \gamma_{ij} < 0 \end{cases}. \tag{6}$$

where τ^Y_{ij} is the initial yield strength, determined by the 0.2% offset strain point.

1.2.2. Damage Initiation

A strain based damage initiation function was used, for simplicity, to model the material response in the longitudinal direction. The failure initiation criterion based on Puck and Schürmann's [14] and Catalanotti et al. [15] was used for predicting matrix damage behaviour. The failure criteria for fibre-dominated and matrix-dominated initiation modes are given as follows,

Fibre-dominated

$$\varepsilon_{11} > 0, \; F^T_{11}(\varepsilon_{11}) = \left(\frac{\varepsilon_{11}}{\varepsilon^{0T}_{11}}\right)^2 \geq 1 \tag{7}$$

$$\varepsilon_{11} < 0, F^C_{11}(\varepsilon_{11}) = \left(\frac{\varepsilon_{11}}{\varepsilon^{0C}_{11}}\right)^2 \geq 1 \tag{8}$$

Matrix-dominated

$$\sigma_{NN} \leq 0, F(\theta) = \left(\frac{\tau_{LN}}{S_{12} - \mu_{LN}\,\sigma_{NN}}\right)^2 + \left(\frac{\tau_{NT}}{S_{23} - \mu_{NT}\,\sigma_{NN}}\right)^2 \tag{9}$$

$$\sigma_{NN} > 0, F(\theta) = \left(\frac{\sigma_{NN}}{S_{23}}\right)^2 + \left(\frac{\tau_{LN}}{S_{12}}\right)^2 + \left(\frac{\tau_{NT}}{S_{23}}\right)^2 + \lambda\left(\frac{\sigma_{NN}}{S_{23}}\right)\left(\frac{\tau_{LN}}{S_{12}}\right)^2 + \kappa\left(\frac{\sigma_{NN}}{S_{23}}\right) \tag{10}$$

Parameters κ and λ are given by $\kappa = S_{23}^2 - (Y^T)^2/S_{23}Y^T$, $\lambda = 2\mu_{LN}S_{23}/S_{12} - \kappa$, S_{12} and S_{23} are the shear strengths.The transverse friction coefficients, defined in [13], are based on Mohr-Coulomb theory where $\mu_{NT} = -1/\tan(2\theta_f)$, $S_{23} = Y^C/2\tan(\theta_f)$ and $\mu_{LN} = \mu_{NT}S_{12}/S_{23}$, Y_C is the transverse compressive strength and the initiation strain $\varepsilon^{0T(C)}_{11} = X^{T(C)}/E_{11}$. The fracture plane orientation, θ_f, is typically found to be approximately 53° for unidirectional composites under uniaxial transverse compressive loading [13] but may assume any orientation under combined loading.

1.2.3. Damage Evolution

As shown in Figure 5, two parameters are introduced to describe the matrix-dominated damage propagation parameter, d_{mat}, under shear loading: (i) shear damage in the strain hardening part, d^I_{ij}, and (ii) shear damage in the strain softening part, d^{II}_{ij}.

$$d_{mat} = d^I_{ij} + d^{II}_{ij}, \tag{11}$$

$$d^I_{ij} = 1 - G^*_{ij}/G^{ini}_{ij}, \tag{12}$$

$$d^{II}_{ij} = d^I_{ij} + \left(1 - d^I_{ij}\right)\frac{\gamma^f_{ij} - \gamma^o_{ij,in}}{\gamma^f_{ij} - \gamma^o_{ij}}\left(\frac{\gamma_{ij} - \gamma^o_{ij}}{\gamma_{ij} - \gamma^o_{ij,in}}\right), \tag{13}$$

where γ_{ij} is the current shear strain, γ^f_{ij} is the final failure shear strain, and $\gamma^o_{ij,in}$ is the inelastic strain at the onset of fracture.

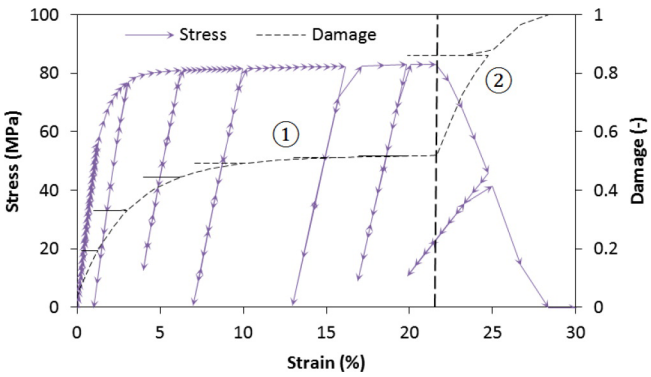

Figure 5. Perfect-plastic stress-strain constitutive law for non-linear shear.

In order to account for irreversibility, the damage variable, as a function of analysis time, *t*, is defined as

$$\begin{cases} d_{mat}(t + \Delta t) = max\{0, min\{1, d_{mat}(t + \Delta t)\}\} \\ d_{mat}(t + \Delta t) \geq d_{ij}(t) \end{cases}, \tag{14}$$

As damage is triggered when the shear strength, τ^o_{ij}, is reached, the response follows a negative tangent stiffness resulting in the softening of the secant shear modulus, with increasing applied strain, to $(1 - d_{mat})G^*_{ij}$, shown by path 3 in Figure 4. Consequently, final failure strain, γ^f_{ij}, is determined by,

$$\gamma^f_{ij} = \frac{2g_{ij}}{\tau^o_{ij}} + \gamma^o_{ij,in}, \tag{15}$$

where $\gamma_{ij,in}^{o}$ is the plastic strain at the onset of failure. Mesh objectivity was achieved by employing the crack-band model of Bažant and Oh [16], where a characteristic length of the finite element (equivalent to a RVE), $g_{ij} = \Gamma_{ij}/l^*$. l^* and the corresponding fracture toughness Γ_{ij} were used. g_{ij} is the volumetric energy release rate associated with elastic fracture energy (red area in Figure 4). A quadratic interpolation function for the fracture energy in the mix-mode case was described in [6] to account for the multidirectional loading cases. An accurate measure of the characteristic length is the ratio of the elemental volume V and fracture plane area A, $l^* = V/A$, described in [6].

A mesh sensitivity study, on a 2mm×2mm×2mm cube loaded in longitudinal tension, was performed with 1^3, 2^3, 3^3, 4^3 and 5^3 elements respectively. The models were loaded in tension longitudinally until complete failure. The response in Figure 6 confirmed the mesh independence of the proposed model as the force-displacement curves of the different meshes were in good agreement except the point close to complete failure. The deviation near complete failure is caused by the difference between the infinitesimal strain used in the model and the finite deformation formulation used in the FE package. This difference is only significant where there are large strains experienced by small elements nearing complete failure.

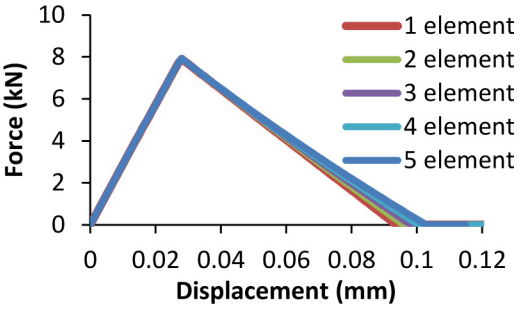

Figure 6. Force-displacement curve for cube model with different mesh densities

1.3. Implementation of Intralaminar Damage Model

The developed intralaminar damage model assesses damage in the two phases of a continuous fibre unidirectional composite ply. Fibre-dominated damage is primarily associated with loading along the fibre direction. The anticipated damage will occur in the form of net fibre breakage in tension and predominantly fibre kink band formation when loaded in compression. Matrix-dominated damage is primarily associated with transverse and shear loading, which leads to plasticity and formation of cracks in the matrix material. The use of a continuum damage mechanics based softening constitutive relationship necessitates the determination of a characteristic length to correctly scale the critical energy release rate.

Element deletion was employed in this model due to the softening nature of the constitutive relationships. An efficient strategy for determining when element deletion is likely to have to be invoked, due to element distortion, is to track the value of the determinant of the Jacobian operator (det **J**) [6] and delete the element if this value approaches zero. As **J** is not available directly from ABAQUS/ VUMAT, and adding this calculation to the subroutine would incur an additional computational cost, the strategy adopted was to interrogate the determinant of the deformation gradient (det **F**) which is available directly from ABAQUS. Det **F** yields the ratio of the deformed, V, and undeformed, V_0, volume of an element,

$$\det \mathbf{F} = \frac{V}{V_0}, \tag{16}$$

and provides a reasonable indication of element distortion. The overall element distortion criterion was subsequently based on both the fibre-dominated longitudinal damage parameter, $d_{11}^{T(C)}$, and limits on det **F** for tracking large changes in element volume,

$$\begin{cases} \text{Delete element if} \\ d_{11}^{T(C)} > 0.99 \\ \det \mathbf{F} < 0.8 \; or \; \det \mathbf{F} > 1.6 \end{cases} \tag{17}$$

The limits on det **F** are user defined and the quoted values were found to yield reliable computational stability.

2. IMPACT AND CAI STRENGTH OF THERMOSET COMPOSITES

Low-velocity impact damage can drastically reduce the residual strength of a composite structure even when the damage is barely visible. The ability to computationally predict the extent of damage and Compression-After-Impact (CAI) strength of a composite structure can potentially lead to the exploration of a larger design space without incurring significant time and cost penalties.

2.1. Material and Method

This section describes the application of the developed material model to simulate a low-velocity impact event follow by a compression-after -impact test. In order to demonstrate the effectiveness of the material model as a virtual testing tool, its performance in predicting the response of impact and residual strength was evaluated against published experimental data [17]. The successful prediction of the quantitative and qualitative responses for these test cases gives confidence in the utility of the model for its intended purpose.

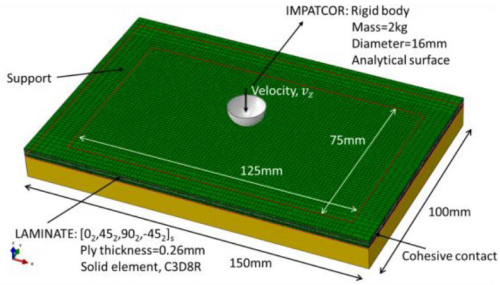

a.

Figure 7. Schematic of (a) Impact and (b) CAI test setup.

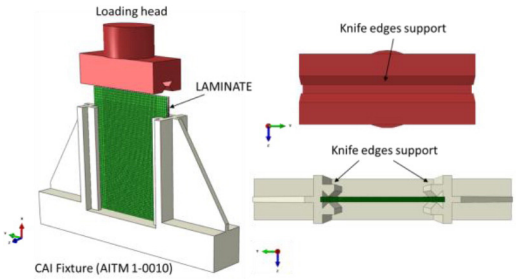

b.

Figure 7. (cont.) Schematic of (a) Impact and (b) CAI test setup.

2.1.1. Impact Test [17]

T700/M21 (see Table 1 for material properties) unidirectional carbon/epoxy laminates $[0_2,45_2,90_2,\text{-}45_2]_s$ were impacted using a drop tower system, with a 16mm diameter, 2kg impactor, following the Airbus Industries Test Method (AITM 1-0010 [18]). The rectangular laminates measured 100×150×4.16mm^3 (ply thickness, t = 0.26 mm) and were placed on a frame of the same size, leaving an inner unsupported region of 75mm×125mm (Figure 7a). The panel was impacted with 29.5J. The impactor was modelled as a spherically-shaped rigid surface, with a reference lumped mass of 2kg. As the lay-up had paired plies, only one element through the thickness of each paired ply was used to reduce computational time.

2.1.2. CAI Test

Once the impact simulation was completed, the damaged specimen was first stabilized by replacing the impact boundary conditions with those representing a picture frame clamped around the specimen to yield a 90mm×130mm test section. The out-of-plane displacements of the nodes, in contact with the picture frame, were constrained to represent a fixed boundary condition (Figure 7b). Although the CAI test is essentially quasi-static (0.5mm/min), it was simulated using ABAQUS/Explicit to avoid the severe convergence difficulties encountered with implicit analysis when modelling highly non-linear behaviour. The load rate was chosen at 3.75m/min to reduce CPU time. Selective mass scaling, which only scaled elements whose stable time increment was below 1e-07s (controlled by the contact algorithm of cohesive surfaces due to the zero-thickness) , was only employed in the CAI process to achieve a reasonable run time.

2.1.3. Material Properties

Material properties for T700/M21 in Table 1 were obtained from [17]. Γ_{jj}^{dir} denotes the longitudinal (jj =11) and transverse (jj=22) intralaminar fracture toughness in tension (dir=T) or compression (dir=C). G_I and G_{II} are the interlaminar fracture toughness for Mode I and Mode II. The mode mixity parameter, η, was determined from experimental measurements provided by Prombut et al.[19] using the method of least squares.

Table 1. Material properties for T700/M21 [17, 20].

Property	Values
Elastic Properties	$E_1 = 130GPa; E_2 = E_3 = 7.7GPa;$ $G_{23} = 3.8GPa;\ G_{12} = G_{13} = 4.8GPa;$ $\nu_{12} = \nu_{13} = 0.3; \nu_{23} = 0.35$
Strength	$X^T = 2080MPa; X^C = 1250MPa; Y^T = 60MPa;\ Y^C = 120MPa;\ S_{12} = 110MPa$
Intralaminar Fracture Toughness	$\Gamma_{11}^T = 133N/mm; \Gamma_{11}^C = 10N/mm; \Gamma_{22}^T = 0.5N/mm; \Gamma_{22}^C = 1.6N/mm; \Gamma_{12} = \Gamma_{23} = \Gamma_{13} = 1.6N/mm;$
Interface Properties	$G_{IC} = 0.5N/mm; G_{IIC} = 1.6N/mm;$ $\eta = 1.45; \tau_3^0 = 20MPa; \tau_{sh}^0 = 36MPa$

2.1.4. FEA Model and Computational Costs

The final FE models each contained a total of 46072 C3D8R elements. Models were run on a Windows Cluster with 32 cores. Each complete simulation (Impact and CAI) took between 19 and 21 hours, depending on impact energy levels. Total simulated time for the impact phase was 4.00e^{-03} s with a time step of 2.00e^{-05} s and a stable time increment of 9.23e^{-09} s. Total simulated time for CAI was 2. 94e^{-03} s with a time step size of 1.47e^{-05} s and a stable time increment of 3.72e^{-07} s.

2.2. Results

The intralaminar damage model allowed the various forms of intralaminar failure to be investigated as the impact event progressed. As shown in Figure 8a and Figure 8b, the impactor force vs. displacement history shows very good agreement in terms of maximum force and global impact response. Fig.1c shows matrix cracking and delamination (modelled using cohesive contact laws) for each double-ply and interface, respectively. The delamination contours shown in Fig. 2c correlate well with results obtained from C-scan studies. CAI intralaminar damage plots for each ply pair and delaminations are shown in Fig.1d. During the CAI process, new delamination and intralaminar matrix damage developed from the impact-induced damage area. Fibre damage was primarily observed in the top and bottom plies. The predicted damage correlated well with experimental findings [17].

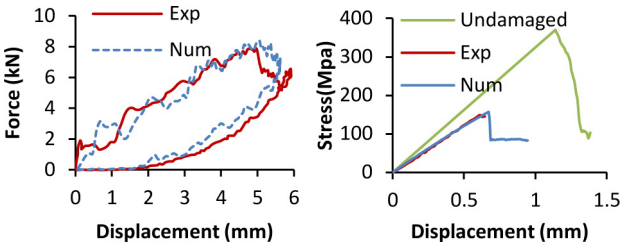

a. b.

Figure 8. (a) Impact response; (b) CAI response; (c) Simulated impact damage contours and (d) Simulated CAI damage contours.

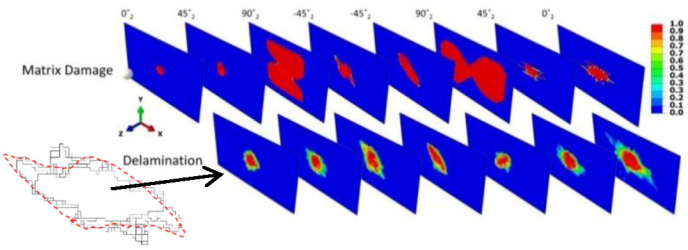

c.

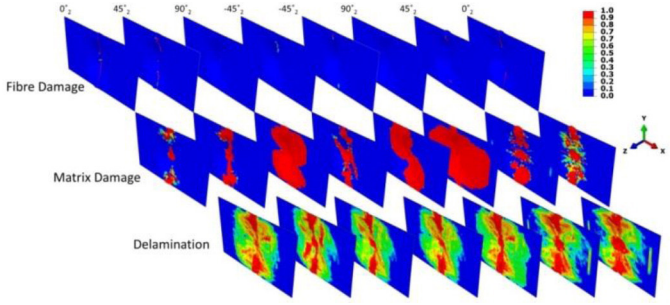

d.

Figure 8. (cont.) (a) Impact response; (b) CAI response; (c) Simulated impact damage contours and (d) Simulated CAI damage contours.

3. CRUSHING OF THERMOSET COMPOSITES SPECIMENS

3.1. Material and Method

A set of laminated wedge specimens were crush-tested by Israr et al. [21] and the results were used to validate the present model. A hydraulic testing machine, at a constant crosshead displacement rate of 6mm/min was used on T700/M21 $[(0°/90°)_4]_s$ specimens with a 20° chamfer angle. The material properties are given in Table 1.

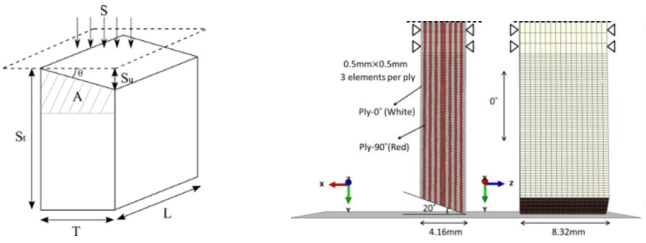

a. b.

Figure 9. Wedge-shaped specimen and finite element model of test set-up

3.2. FEA Model Definition and Computational Costs

Virtual wedge-shaped specimens were created in ABAQUS/Explicit 6.12. The non-clamped part was meshed using an approximate element size of 0.25mm in the longitudinal and transverse directions as shown in Figure 9, while for the clamped part the mesh size was approximately 2mm. In order for C3D8R elements to capture the bending behaviour, three elements through the thickness of each ply were used. To suppress spurious energy modes, an enhanced stiffness-based hourglass and distortion control were employed.

The surface based cohesive behaviour was employed to capture delamination between adjacent plies. A general contact algorithm was utilised to generate a contact force between contact surfaces. 'Hard' contact conditions were defined between the platen and the plies as well as adjacent plies. The platen was modelled as an analytical rigid surface. The friction coefficients were set to 0.2 for T700/M21. The computational loading speed was fixed at 1m/s to reduce the CPU time whilst ensuring that the quality of the results was not affected by inertial effects. Selective mass scaling, which only scaled elements whose stable time increment was below 1e-07s, was also employed during the crushing process to achieve a reasonable run time. Models were run on a Windows Cluster with 16 CPUs with a run time of between 6 and 8 hours, depending on the specimen type. Total simulation time for CAI is $1e^{-02}$ s, time step size is $5e^{-05}$ s and stable incremental time is around $9.5e^{-08}$ s.

3.3. Results

The global force-displacement response (Figure 10a) further confirms the quantitative accuracy of the present damage model. The numerical oscillations are the result of element deletion laws invoked as part of the solution. The evolution of energy dissipated through various mechanisms during crushing is illustrated in Figure 10b. The majority of energy was dissipated through intralaminar damage, followed by friction between the crushing platen and specimen, and delamination. The numerical results in Figure 10c achieved excellent correlation with the experimental crushing morphologies. Internal debris was created and acted like a 'wedge' in driving delamination.

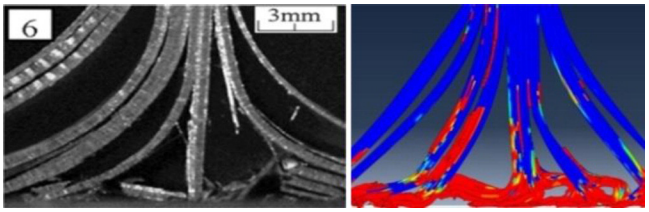

a.

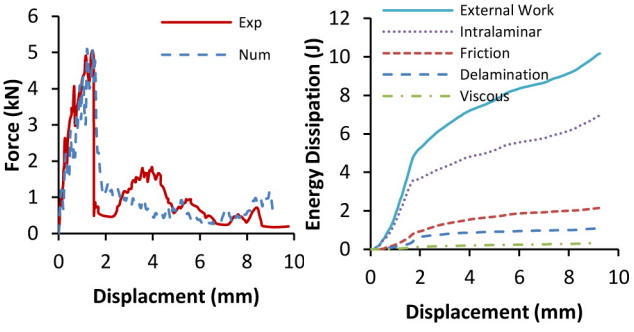

b. c.

Figure 10. (a) Experimental morphologies [21] and numerical matrix damage contour; (b) force-displacement curve of crushing test on [(0˚/90˚)4]s specimen; (c) energy dissipation- displacement curves.

4. CRUSHING OF THERMOPLASTIC COMPOSITES

Corrugated webs manufactured with carbon fibre (CF)/Epoxy have been used for several energy-absorbing applications in helicopter sub-floor [22] and aircraft fuselage structures [23]. The self-support nature of corrugated composite structures doesn't require any specialized test fixtures, hence removing the possibility of such fixtures influencing the crush behaviour of the specimen [24]. Not only do such structures display greater stability under loading, but they are also relatively easy to manufacture, compared to tubular specimens, using compression moulding, thermoforming or injection moulding techniques. Very limited research work has been conducted on thermoplastic composite structures made of corrugated webs. The high fracture toughness associated with thermoplastic composites implies that they have great potential in improving the crashworthiness performance of composite automotive structures.

4.1. Materials and Method

The fibre reinforced composite material used in this study is manufactured from unidirectional carbon fibre (AS4D 12K) / poly-ether-ketone-ketone (PEKK) pre-preg tape provided by Cytec Engineered Materials®. Cross-ply $[0/90]_{3s}$ AS4/PEKK composite corrugated samples with 12 plies were fabricated using a Collin® compression moulding machine in a consolidation cycle as per the manufacturer's specifications. The specimen denoted as 'Semi-3p' has semi-circular corrugations where 'p' denotes the number of semicircles or 'half-waves'. The 'Hat-3p' specimens have three semi-hexagonal segments. All three shapes have end-lips on each side for additional stability. The dimensions of each segment are specified in Figure 11. The specimens were tested in compression between two flat steel platens in a Hounsfield machine with a 50kN load cell. The force response was recorded directly from the load cell while the displacement was obtained from the moving crosshead. The crosshead speed was set at 5mm/min, giving a nominal strain rate of $1 \times 10^{-3}/s$.

Double-cantilever-beam (DCB) [25], four-point end-notched flexure (4ENF) [26] and Mixed-mode bending (MMB) [27] test configurations were used to determine initiation/propagation fracture toughness of mode I, mode II and mixed-mode respectively. Compact Tension (CT) and Compact compression tests (CC) [28, 29] were employed to measure the longitudinal tensile and compressive fracture toughness. V-notched rail shear tests were employed to measure the non-linear behaviour and fracture toughness associated with shear loading [30]. The measured values from [31] given in Table 2 were then used as input material parameters to model the crushing behaviour Verifications were also carried out by simulating the material characterization test themselves. Finite element analysis based on the proposed composite damage model accurately predicted interlaminar and intralaminar failure modes of composite laminates both qualitatively and quantitatively.

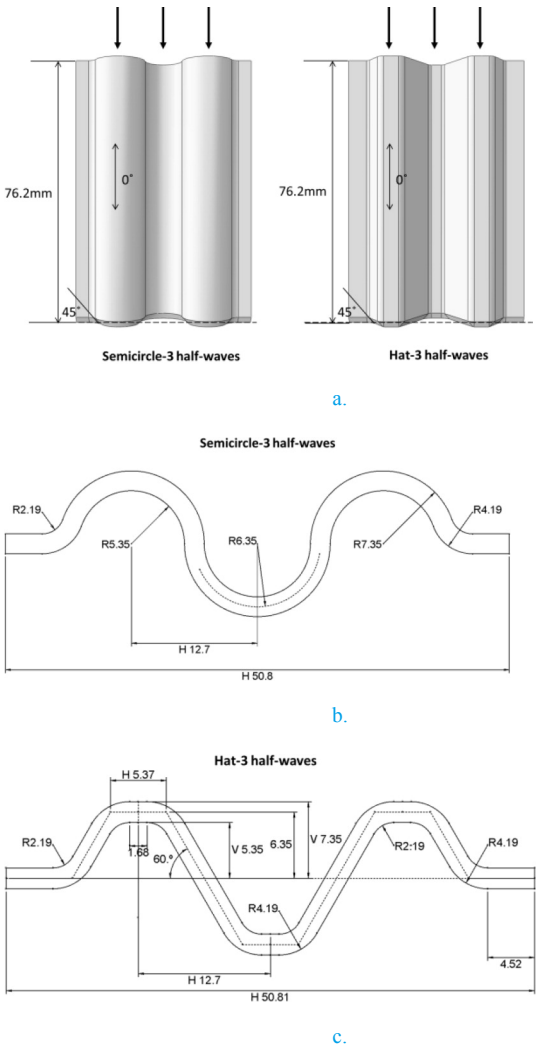

Figure 11. Specimen geometries (a) chamfer and loading direction and (b) cross-section dimensions (mm).

4.2. FEA Model Definition and Computational Costs

The geometry was meshed using an approximate element size of 0.5mm in the longitudinal (crush direction) and 1mm in the transverse directions. In order for C3D8R elements to capture the bending behaviour, three elements through the thickness of each ply were used. To suppress spurious energy modes, an enhanced stiffness-based hourglass and distortion control were employed. The surface based cohesive behaviour was employed to capture delamination between adjacent plies. A general contact algorithm was utilised to generate a contact force between contact surfaces. 'Hard' contact conditions were defined between the platen and the plies as well as adjacent plies. The platen was modelled as an analytical rigid surface. The friction coefficients of ply-to-ply and ply-to-metal contact were set to 0.28 and 0.2 respectively, measured in [32]. The computational loading speed was fixed at 1m/s to reduce the CPU time whilst ensuring that the quality of the results was not affected by inertial effects. Selective mass scaling, which only scaled elements whose stable time increment was below 5e-08s, was also employed during the crushing process to achieve a reasonable run time. Low-pass filters were employed to remove the numerical oscillations as an artefact of explicit dynamic modelling. Models were run on a

Windows Cluster with 16 CPUs with a run time of between 32 and 40 hours, depending on the specimen type. Total simulation time for CAI is $1e^{-03}$ s, time step size is $5e^{-05}$ s and stable incremental time is around $4.6e^{-08}$ s.

Table 2. Material properties for AS4/PEKK thermoplastic composites

Material Property	Values
Elastic Properties (ply)	$E_{11} = 139GPa; E_{22} = E_{32} = 10.3GPa; G_{23} = 5.2GPa; G_{12} = G_{13} = 5.2GPa; \nu_{12} = \nu_{13} = 0.3; \nu_{23} = 0.3$
Strength	$X^T = 2463MPa; X^C = 1493MPa; Y^T = 102MPa; Y^C = 206MPa;$ [33] $S_{12} = S_{13} = 82MPa$
Fracture toughness	$\Gamma_{11}^T = 243.9N/mm; \Gamma_{11}^C = 108.3N/mm; \Gamma_{22}^T = 1.564N/mm; \Gamma_{22}^C = 34.58N/mm; \Gamma_{12} = \Gamma_{23} = \Gamma_{13} = 34.48N/mm;$
Shear coefficients	$\tau_{ij}^Y = 80.81MPa; \alpha = 0.16; \beta = -44.26;$
Degraded modulus coefficients	$p_1 = 2405; p_2 = -32.59; p_3 = 2596; p_4 = -0.1764$
Interface properties	$G_{Ic} = 1.564N/mm; G_{IIc} = 2.113N/mm; \eta = 0.996; \tau_1^0 = 98MPa; \tau_{2(3)}^0 = 60MPa; k = 1 \times 10^6$

4.2. Results

4.2.1. Semi-3p

At the beginning of the crushing process (stage 1), damage was primarily in the form of local fragmentation as the trigger region was consumed. The reaction force increased gradually to the peak load at which point the entire uniform cross-section of the crush element came in contact with the platen (displacement around 2.4-2.7mm). In the second stage, delamination initiated with a splaying mode accompanied by extensive fibre tensile and compressive breakage in the high-curvature area (highlighted in Figure 13c and Figure 14c), leading to a sudden drop in the reaction force as the chamfer was being consumed. From stage 3 to stage 6, the outer plies deform in bending while the inner plies tend to undergo crushing, as shown in Figure 12-3c. Internal debris was also created and acted like a 'wedge' in driving delamination.

The numerical results in Figure 13a and Figure 14a achieved excellent quantitative correlation with experimental data without the need of calibrating any of the input data. The initial stiffness, peak force (F_P) and steady-state force (F_{SS}) were all captured by the numerical model, which is consistent with the range of observed experimental results. The displacement at which the peak force occurred was predicted with good accuracy. The sudden load drop after the peak force is attributed to extensive delamination after the chamfer trigger was fully consumed. The progressive nature of the crushing was well captured, with a clear force plateau during the steady state crushing. The overall numerical oscillations are the result of element deletion laws invoked as part of the solution and artefacts of explicit dynamic simulation.

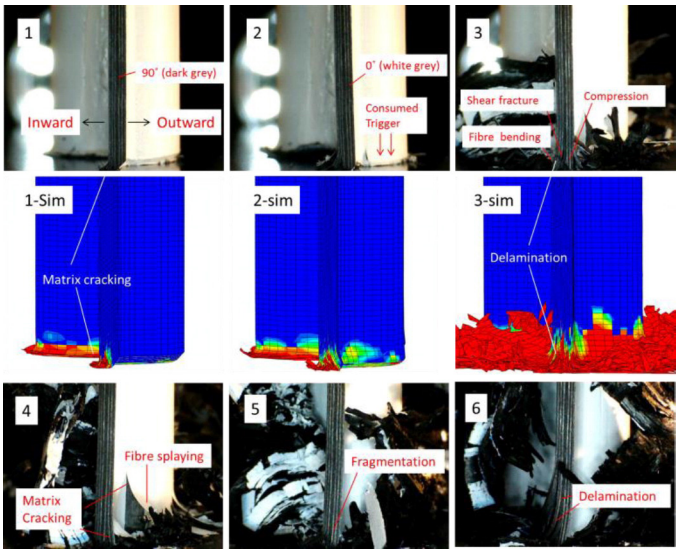

Figure 12. Failure process at 6 stages from side view

The numerical results, from Figure 13b and Figure 14b, showing the crushing morphology confirm the qualitative accuracy of the present damage model. Matrix cracking, shear fracture, delamination, ply bending and fragmentation were well predicted. The virtual formation of fronds around the circumference shows excellent qualitative similarity when compared with experimental results (Figure 13c and Figure 14c).

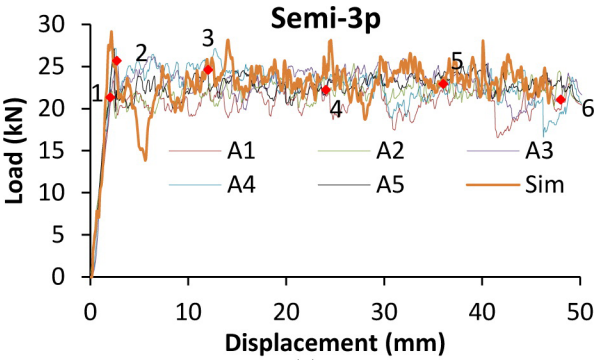

a.

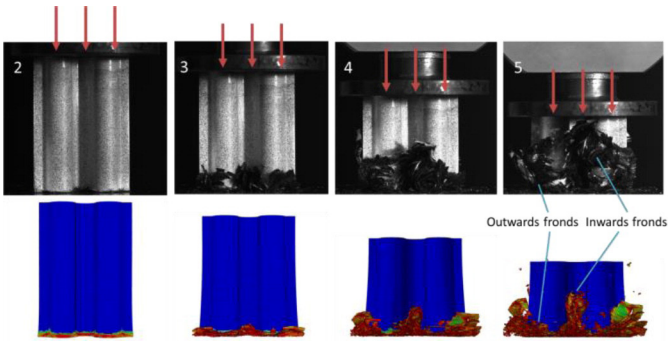

b.

Figure 13. (a) Force-displacement curve; (b) Front view and (c) Top view of experimental and numerical matrix damage; (d)Energy dissipation mechanisms of Semi-3p

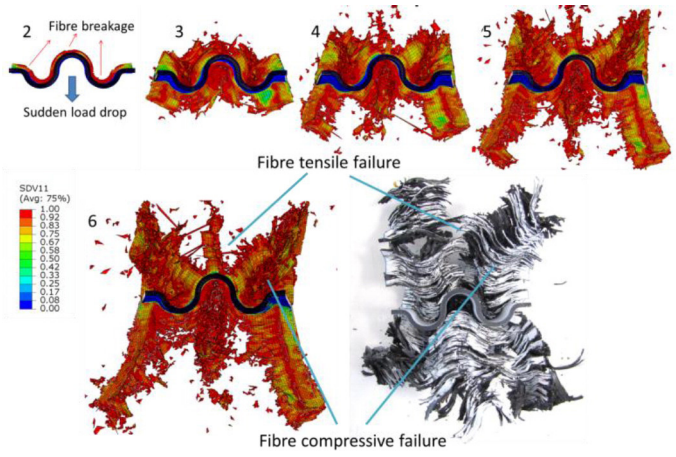

c.

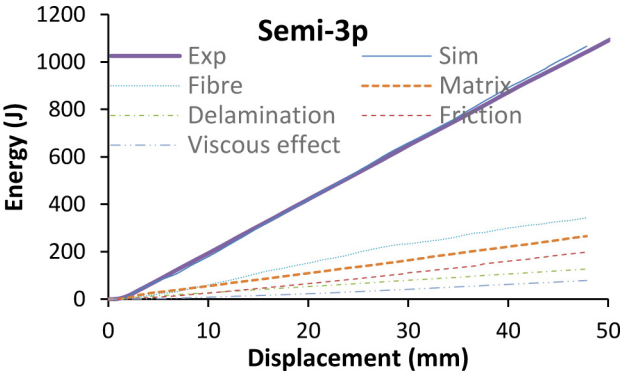

d.

Figure 13. (cont.) (a) Force-displacement curve; (b) Front view and (c) Top view of experimental and numerical matrix damage; (d)Energy dissipation mechanisms of Semi-3p

4.2.2. Hat-3p

The evolution of energy dissipated through various mechanisms during crushing is illustrated in Figure 13 and Figure 14 for all the corrugated structures tested, verifying the energy balance relationship between external work done and energy absorbed. The predicted total energy dissipated was in good agreement with the experimental total absorbed energy. The majority of energy was dissipated through intralaminar damage combining fibre tensile /compressive damage (e.g. 34.4% in Semi-3p) and matrix tensile/compression/shear damage (e.g. 23.5% in Semi-3p), followed by the friction between the crushing platen and specimen and internal friction between the plies (e.g. 15.1% in Semi-3p). Extensive delamination (green line) contributed approximately 12.8% (Semi-3p) of the total energy dissipation. The small amount of viscous energy dissipated is due to the use of the bulk viscosity method to damp out spurious oscillations in explicit dynamic simulations. Most of the energy was dissipated in a steady-state fashion as progressive failure occurred.

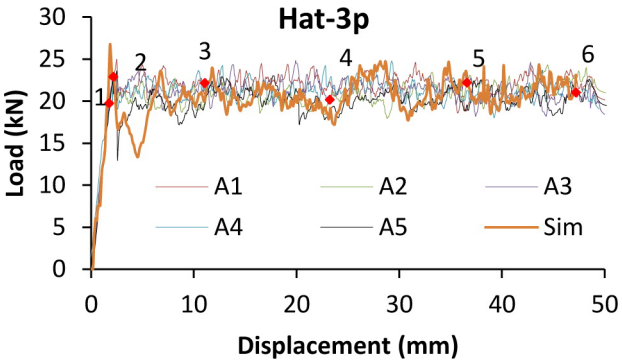

a.

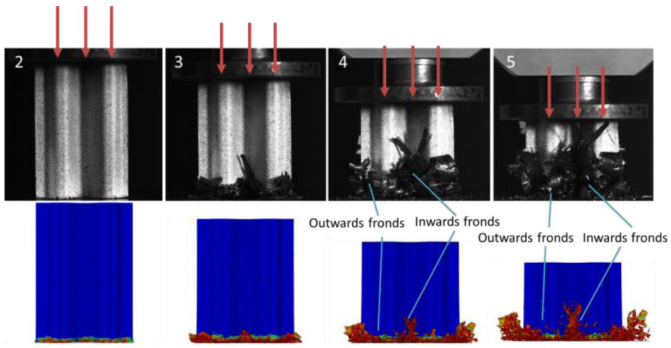

b.

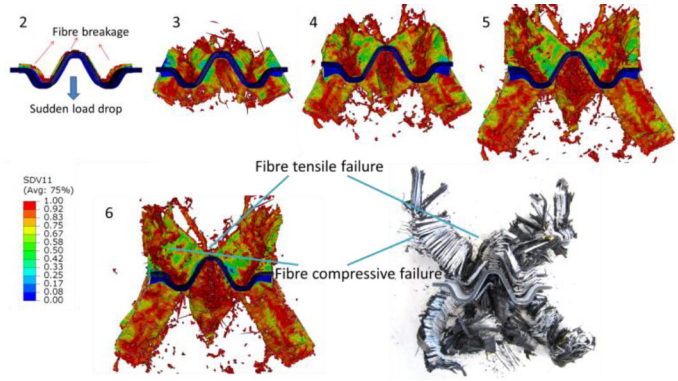

c.

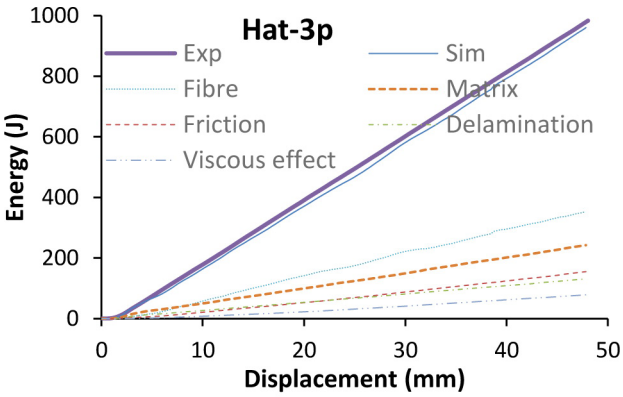

(d)

d.

Figure 14. (a) Force-displacement curve; (b) Front view and (c) Top view of experimental and numerical matrix damage; (d)Energy dissipation mechanisms of Semi-3p

4.2.3. Crashworthiness Assessment

The performance of crashworthy composite structures can be evaluated by their total energy absorption (E_s), specific energy absorption (SEA), peak force (F_P), steady-state force (F_{SS}) and crush efficiency (CE). The total energy absorption, E_s, is the area under the force (F) -displacement (S) curve. SEA is defined as the energy absorbed per unit mass of material, $SEA = \int FdS/m$, which is a critical assessment of performance for lightweight structures which may be used in aircraft or road vehicles. F_P is the highest force experienced during the crush event and has a direct correlation with the extent of potential injury to passengers. F_{SS} is the mean force during steady-state crushing of the specimen and is an indicator of the energy absorption capability of crashworthy structures. Crush efficiency CE is the ratio between F_{SS} and F_P indicating the nature of the crush response. A high-energy absorbing crashworthy structure is characterised by progressive failure where the peak force is not much higher than the steady-state force, i.e. one with high crush efficiency.

The average crashworthiness performance results, for different types of corrugated structures, are presented in Table 3. The SEA and mean crush stress of Semi-3p and Hat-3p corrugated structures was found to yield a very similar trend, since they can be related by the material density, $SEA = \int FdS/m = F_{SS}S/\rho AS = \bar{\sigma}/\rho$. Semi-3p has a higher SEA of 110.12 kJ/kg. This can be compared to identical corrugated structures but made of CF/epoxy tested by Feraboli [24], where the value was reported as 70 kJ/kg for regular epoxy and 93 kJ/kg for toughened epoxy. The SEA of AS4/PEKK shows an increase of 57.3% and 18.4% respectively, indicating significant crashworthiness performance improvement of thermoplastic composite structures compared to their thermoset counterparts. This is primarily due to the superior interlaminar fracture toughness of thermoplastics compared to thermoset matrix materials [1]. Crush efficiency of different shapes in both Semi-3p and Hat-3p was around 0.9, indicating that all these structures can achieve high crush efficiency regardless of shapes and periods.

Table 3. Results of crashworthiness performance (S.D.: standard deviation)

Performance metrics	Semi-3p	S.D.	Hat-3p	S.D.
EA (kJ)	1090.22	39.26	1035.93	28.71
SEA (kJ/kg)	110.12	3.97	105.17	2.91
Peak force (kN)	25.05	2.04	23.64	0.92
Steady force (kN)	22.39	0.81	21.12	0.60
Mean crush stress (MPa)	175.74	6.39	167.54	4.78
Crush efficiency (-)	0.90	0.06	0.89	0.03

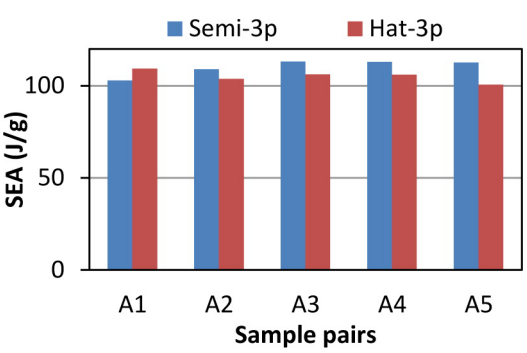

Figure 15. Comparison of specific energy absorption

A comparison of SEA for individual specimen pairs (one Semi-3p and one Hat-3p produced from a single panel) is shown in Figure 15. Although there are some variations between each test pair, Semi-3p shows a slightly higher SEA among all the pairs except the A1 p.

CONCLUSIONS

This paper has outlined recent progress in the development of finite-element-based predictive modelling tools for capturing impact damage, residual strength and energy absorption of thermoset and thermoplastic composites for crashworthiness assessments.

A mesoscale damage model combined a range of novel features with established techniques to accurately capture the material response under damaging loads. The developed model fulfils this requirement by providing accurate and detailed modelling capability using intrinsic ply-level material properties that do not require calibration to obtain good correlation. Future work will focus on extending this computational damage model to capture strain rate effects which will enable accurate assessments of crashworthiness of composite structures in high energy crash events.

REFERENCES

1. Jacob, G.C., et al., *Energy absorption in polymer composites for automotive crashworthiness*. J Compos Mater, 2002. 6(7): p. 813-850.
2. Bisagni, C., et al., *Progressive crushing of fiber-reinforced composite structural components of a Formula One racing car*. Compos Struct, 2005. 68(4): p. 491-503.
3. Ostergaard, M.G., et al., *Virtual testing of aircraft structures*. CEAS Aeronautical Journal, 2011. 1(1-4): p. 83-103.
4. Rouchon, J., *Certification of large airplane composite structures*, in *Recent progress and new trends in compliance philosophy*. ICAS 1990. p. 1439-1447.
5. Tan, W., Falzon B.G., and Price M., *Predicting the crushing behaviour of composite material using high-fidelity finite element modelling*. International Journal of Crashworthiness, 2015. 20(1): p. 60-77.
6. Tan, W., et al., *Predicting low velocity impact damage and Compression-After-Impact (CAI) behaviour of composite laminates*. Composites Part A: Applied Science and Manufacturing, 2015. 71(0): p. 212-26.
7. Falzon, B.G. and Apruzzese P., *Numerical analysis of intralaminar failure mechanisms in composite structures. Part II: Applications*. Compos Struct, 2011. 93(2): p. 1047-1053.
8. Falzon, B.G. and Apruzzese P., *Numerical analysis of intralaminar failure mechanisms in composite structures. Part I: FE implementation*. Compos Struct, 2011. 93(2): p. 1039-1046.
9. Faggiani, A. and Falzon B.G., *Predicting low-velocity impact damage on a stiffened composite panel*. Composites Part A: Applied Science and Manufacturing, 2010. 41(6): p. 737-749.
10. Systems, D. ABAQUS Documentation 6.12. 2012
11. Benzeggagh, M.L. and Kenane M., *Measurement of mixed-mode delamination fracture toughness of unidirectional glass/epoxy composites with mixed-mode bending apparatus*. Composites science and technology, 1996. 56: p. 439-449.
12. Camanho, P.P. and Davila C.G., *Mixed-mode decohesion finite elements for the simulation of delamination in composite materials*. NASA-Technical Paper, 2002. 211737(1): p. 33.
13. Lemaitre, J. and Chaboche J.-L., *Mechanics of solid materials*. 1994: Cambridge university press.
14. Puck, A. and Schürmann H., *Failure analysis of FRP laminates by means of physically based phenomenological models*. Compos Sci Technol, 1998. 58(7): p. 1045-1067.
15. Catalanotti, G., Camanho P.P., and Marques A.T., *Three-dimensional failure criteria for fiber-reinforced laminates*. Composite Structures, 2013. 95(0): p. 63-79.
16. Fleming, D.C., *Modelling composite crushing initiation using a cohesive element formulation*. Int J Crash, 2011. 16(5): p. 475-485.

17. Rivallant, S., Bouvet C., and Hongkarnjanakul N., *Failure analysis of CFRP laminates subjected to compression after impact: FE simulation using discrete interface elements*. Composites Part A: Applied Science and Manufacturing, 2013. 55: p. 83-93.
18. Method, A.I.T. Determination of Compression Strength after Impact. 2010
19. Prombut, P., et al., *Delamination of multidirectional composite laminates at 0°/θ° ply interfaces*. Engineering Fracture Mechanics, 2006. 73(16): p. 2427-2442.
20. Hongkarnjanakul, N., Bouvet C., and Rivallant S., *Validation of low velocity impact modelling on different stacking sequences of CFRP laminates and influence of fibre failure*. Composite Structures, 2013. 106(0): p. 549-559.
21. Israr, H.A., Rivallant S., and Barrau J.J., *Experimental investigation on mean crushing stress characterization of carbon-epoxy plies under compressive crushing mode*. Compos Struct, 2013. 96(0): p. 357-364.
22. Waimer, M., et al., *Experimental study of CFRP components subjected to dynamic crash loads*. Composite Structures, 2013. 105: p. 288-299.
23. Heimbs, S., Strobl F., and Middendorf P., *Integration of a Composite Crash Absorber in Aircraft Fuselage Vertical Struts*. International Journal of Vehicle Structures & Systems, 2011. 3(2): p. 87-95.
24. Feraboli, P., *Development of a corrugated test specimen for composite materials energy absorption*. J Compos Mater, 2008. 42(3): p. 229-256.
25. ASTM. D5528-13. Standard Test Method for Mode I Interlaminar Fracture Toughness of Unidirectional Fiber-Reinforced Polymer Matrix Composites. West Conshohocken, PA 2013
26. Offringa, A., et al. *Fiber reinforced thermoplastic butt joint development*. in Proceedings of International SAMPE Symposium and Exhibition. 2008.
27. ASTM. D6671/D6671M-13e1. Mixed Mode I-Mode II Interlaminar Fracture Toughness of Unidirectional Fibre Reinforced Polymer Matrix Composites. West Conshohocken, PA. 2013
28. Jose, S., et al., *Intralaminar fracture toughness of a cross-ply laminate and its constituent sub-laminates*. Composites Science and Technology, 2001. 61(8): p. 1115-1122.
29. Pinho, S.T., Robinson P., and Iannucci L., *Fracture toughness of the tensile and compressive fibre failure modes in laminated composites*. Composites Science and Technology, 2006. 66(13): p. 2069-2079.
30. ASTM. D7078/D7078M-12. Standard Test Method for Shear Properties of Composite Materials by V-Notched Rail Shear Method. West Conshohocken, PA. 2012
31. Tan, W., Falzon B.G., and Liu H., *Detailed material characterization and modelling of the failure modes of unidirectional AS4/PEKK thermoplastic composite plies*. 2015. **Submitted**.
32. Tan, W. and Falzon B.G., *Modelling the nonlinear behaviour and fracture process of AS4/PEKK thermoplastic composite under shear loading*. 2015. **Submitted**.
33. Vogler, T.J. and Kyriakides S., *Inelastic behavior of an AS4/PEEK composite under combined transverse compression and shear. Part I: experiments*. International Journal of Plasticity, 1999. 15(8): p. 783-806.

CONTACT INFORMATION

Corresponding author:
b.falzon@qub.ac.uk
(B.G. Falzon)
Tel: +44(0)28 9097 5640
School of Mechanical and Aerospace Engineering
Queen's University Belfast, Belfast, BT9 5AH, UK

ACKNOWLEDGMENTS

The corresponding author would like to acknowledge the financial support of Bombardier and the Royal Academy of Engineering. The authors would also like to gratefully acknowledge the funding from the Queen's University Belfast/China Scholarship Council (QUB/CSC) PhD Scholarship and the support from the Research Computing Team at QUB in accessing the HPC facilities.

ABBREVIATIONS

CAI - Compression after impact

SEA - Specific energy absorption

PEKK - Poly-ether-ketone-ketone

CE - Crush efficiency

CF - Carbon fibre

S.D. - Standard deviation

RVE - Representative volume element

Semi - Semicircle

3p - 3 half-waves